

Article

Modified NiMo Nanoparticles for Efficient Catalytic Hydrogen Generation from Hydrous Hydrazine

Ying Liu ^{1,2,3,4}, Huan Zhang ⁴, Cong Ma ^{4,*} and Nan Sun ^{5,*}¹ School of Chemical Engineering and Technology, Tianjin University, Tianjin 300072, China² National Engineering and Research Centre of Distillation Technology, Tianjin University, Tianjin 300072, China³ Peiyang National Distillation Technology Engineering Company Limited, Tianjin 300072, China⁴ State Key Laboratory of Separation Membranes and Membrane Processes, School of Environmental Science and Engineering, Tianjin Polytechnic University, Tianjin 300387, China⁵ School of Water Conservancy and Civil Engineering, Northeast Agricultural University, Harbin 150030, China

* Correspondence: macong_0805@126.com (C.M.); sunnan@neau.edu.cn (N.S.)

Received: 30 April 2019; Accepted: 2 July 2019; Published: 10 July 2019



Abstract: Precious metal-free NiMoM (M = Pr₂O₃, Cu₂O) catalysts have been synthesized through a simple coreduction method, without any surfactant or support material, and characterized using X-ray diffraction (XRD), transmission electron microscopy (TEM), and X-ray photoelectron spectroscopy (XPS). The resultant Pr₂O₃- or Cu₂O-modified NiMo catalysts exhibit different structures, which is due to a difference in the synergistic effects of NiMo and the modifying elements. NiMoPr₂O₃ has an amorphous structure, with low crystallinity and uniform particle dispersion, while NiMo@Cu₂O adopts the core-shell structure, where the core and shell are synergistic with each other to promote electron transfer efficiency. The support material-free nanocatalysts Ni₉Mo₁(Pr₂O₃)_{0.375} and Ni₄Mo@Cu₂O are both highly efficient compared with bimetallic NiMo catalysts, in terms of hydrogen generation from hydrous hydrazine (N₂H₄·H₂O) at 343 K, with total turnover frequencies (TOFs) of 62 h⁻¹ and 71.4 h⁻¹, respectively. Their corresponding activation energies (E_a) were determined to be 43.24 kJ mol⁻¹ and 46.47 kJ mol⁻¹, respectively. This is the first report on the use of Pr-modified NiMo and core-shell NiMo@Cu₂O catalysts, and these results may be used to promote the effective application of noble metal-free nanocatalysts for hydrogen production from hydrous hydrazine.

Keywords: NiMoM (M = Pr₂O₃, Cu₂O) catalysts; hydrous hydrazine; hydrogen production

1. Introduction

It is expected that energy consumption and associated environmental issues will continue to grow dramatically in the near future. As an environmentally friendly fuel, hydrogen has the advantages of high combustion heat and high combustion speed. In addition to generating water and a little hydrogen azide during the combustion process, it will not produce substances that are harmful to the environment such as carbon oxides and hydrocarbons compounds. Hydrogen has been proposed as crucial to ensuring secure and sustainable energy development [1–3]. However, the search for effective hydrogen storage materials and methods for hydrogen generation remains a challenge.

In recent years, chemical hydrogen storage has become a popular approach to overcoming the barriers of hydrogen delivery. Hydrous hydrazine (N₂H₄·H₂O), which is a liquid at room temperature, is a promising hydrogen carrier due to its relatively low cost, high hydrogen density (8.0 wt. %), low molecular weight (50.06 g mol⁻¹) [4,5], and the advantages of only producing H₂ and N₂ in its decomposition reactions (pathway 1: N₂H₄ → N₂ + 2H₂). However, to maximize the usability of

$N_2H_4 \cdot H_2O$ in hydrogen storage, we should avoid the undesirable generation of ammonia (pathway 2: $3N_2H_4 \rightarrow N_2 + 4NH_3$). Although ammonia can be burned, not only generates less heat than that of H_2 as fuel, but also produces harmful gases like NO. Catalysis plays a critical role in the design of efficient processes and systems able to exploit the advantages of the starting materials, while minimizing waste generation and energy requirements [6]. Several recent studies found that Ni-based catalysts promoted by noble metals, such as Ni-Rh [7–9], Ni-Pt [10–13], Ni-Pd [14–16], and Ni-Ir exhibit superior catalytic performances in the decomposition of hydrous hydrazine, with more than 90% H_2 selectivity [17,18]. In fact, although nanocatalysts formed from noble metals and nickel exhibit good catalytic performance, high associated costs limit their use. Other studies have therefore employed nonprecious metals instead of precious metals. He et al. [19] modified Ni nanoparticles with a small amount of CeO_2 (8.0 mol %), resulting in significant enhancement of the turnover frequency (TOF) and H_2 selectivity. Men et al. [20] synthesized catalysts using CeO_x -modified NiFe deposited on reduced graphene oxide (rGO), which exhibited good catalytic characteristics. Manukyan et al. [21] selected copper nanoparticles as the support material, and synthesized a NiFe/Cu catalyst. Copper may be an efficient support material for nickel in the water–gas shift reaction, as it shows high activity and stability. Wang et al. [22] successfully synthesized a $Cu@Fe_5Ni_5$ catalyst, which exhibited high activity in terms of complete $N_2H_4 \cdot H_2O$ decomposition. This is due to the electronic coupling between the core and shell metals. Noble metal-free modified Ni-based catalysts not only facilitate the use of N_2H_4 as a chemical hydrogen-producing material, but also provide a potential development path for more rare earth-doped catalysts.

Yang et al. [23] reported that a NiMo catalyst catalyzed the hydrogen production of ammonium borane, and that the electronic interactions between the NiMo enable the catalyst to achieve complete decomposition of the ammonia borane within 2 min. We report a simple coreduction method for preparing NiMo catalysts, which are modified with rare earth elements and nonprecious metals under room temperature, without any support material or surfactant. Pr and Ce are the same as lanthanides elements, with similar chemical structures and properties, although most studies employ Ce as the raw material. In order to further evaluate the value of rare earth elements and their wide application, we employed a Pr-modified NiMo catalyst. As a transition metal, Cu is often the main active element in catalysis. A Cu-modified NiMo catalyst is used to synergize the elements to further improve catalytic performance, and the catalytic properties of the $Ni_{1-x}Mo_x(Pr_2O_3)_y$ and $Ni_{1-x}Mo_x@(Cu_2O)_y$ materials are investigated and compared. The effects of reaction temperature, concentrations of NaOH, and the kinetics of $N_2H_4 \cdot H_2O$ decomposition are also evaluated in this work.

2. Results and Discussion

2.1. Physical Characteristics of $Ni_{1-x}Mo_x(Pr_2O_3)_y$ and $Ni_{1-x}Mo_x@(Cu_2O)_y$ Nanocatalysts

The one-pot coreduction process provides simple, effective, and readily scalable preparation of nanocatalysts. In the present study, we employ this method to prepare a series of $Ni_{1-x}Mo_x(Pr_2O_3)_y$ and $Ni_{1-x}Mo_x@(Cu_2O)_y$ catalysts, where x represents the molar portion of Mo and y represents the molar portion of the third material (Cu_2O or Pr_2O_3). It should be noted that in the preparation of catalysts, the total masses of Ni and Mo are controlled, to a certain extent. After the modification of the NiMo catalysts, $Ni_9Mo_1(Pr_2O_3)_y$ and $Ni_8Mo_2@(Cu_2O)_y$ refer to the $Ni_{0.9}Mo_{0.1}(Pr_2O_3)_y$ and $Ni_{0.8}Mo_{0.2}@(Cu_2O)_y$ nanocatalysts.

X-ray diffraction (XRD) is used to analyze the crystalline structures of the prepared catalysts. Figure 1a presents the XRD patterns of $Ni_9Mo_1(Pr_2O_3)_y$ and the bimetallic $Ni_{0.2}Pr_{0.015}$, $Mo_{0.2}Pr_{0.015}$, and Ni_9Mo_1 catalysts. The diffraction peak of Ni (PDF#04-0850) was detected in all the catalyst samples, with the exception of the $Mo_{0.2}Pr_{0.015}$ catalyst, at $2\theta = 44.5^\circ$, corresponding to the Ni(111) crystal plane peak. The face-centered cubic (FCC) configuration of nickel has three crystal faces—(111), (200), and (220)—and here the diffraction peak only corresponds to the (111) crystal plane, indicating that the prepared catalysts have low crystallinity and are a mixture of crystalline and amorphous structures.

Compared with the Ni_9Mo_1 catalyst, $\text{Ni}_9\text{Mo}_1(\text{Pr}_2\text{O}_3)_y$ showed much weaker Ni peaks, with the (111) peak intensities of the $\text{Ni}_9\text{Mo}_1(\text{Pr}_2\text{O}_3)_y$ samples decreasing gradually with increasing Pr_2O_3 content. This suggests that the incorporation of Pr into the catalyst may perturb the crystal growth of the Ni nanocrystallite. When the doping ratio of Pr reaches 0.375, the diffraction peaks of Ni are no longer weakened, which indicates that the catalysts of $\text{Ni}_9\text{Mo}_1(\text{Pr}_2\text{O}_3)_y$ can reach a point where there is a coexistence of crystalline and amorphous states, under optimal conditions [21,22]. However, as shown in Figure 1b, the XRD pattern of $\text{Ni}_8\text{Mo}_2@(\text{Cu}_2\text{O})_y$ contains prominent diffraction peaks at $2\theta = 36.4^\circ$, 41.3° , 61.3° , and 73.5° , which can be indexed to diffractions of the (111), (200), (220), and (311) planes of Cu_2O (PDF#05-0667), respectively. The diffraction peaks of Cu_2O strengthened with increasing Cu content. According to the transmission electron microscope (TEM) data (Figure 2f), Cu_2O forms a crystalline state on the outer layer of the catalyst, while internal NiMo crystallinity is low, and so no diffraction peak is observed for Ni. These results clearly indicate that the $\text{Ni}_8\text{Mo}_2@(\text{Cu}_2\text{O})_y$ alloy nanocatalyst is not a simple physical mixture of individual metal nanoparticles, but a coupling between the shell and the nucleus [24].

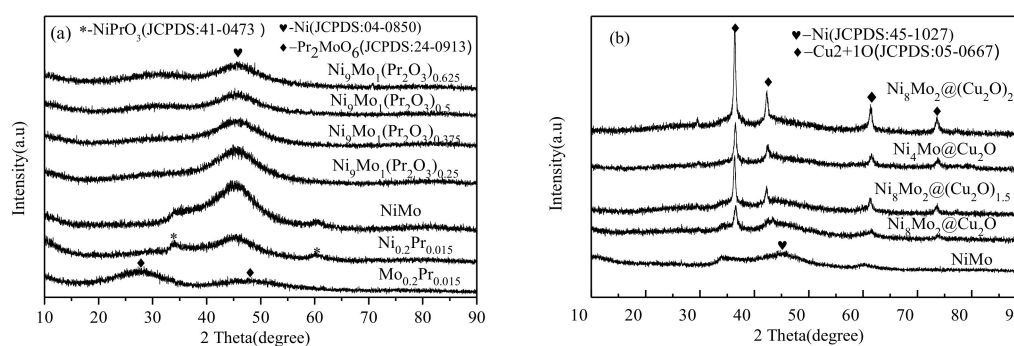


Figure 1. (a) XRD patterns of $\text{Ni}_9\text{Mo}_1(\text{Pr}_2\text{O}_3)_y$ ($y = 0, 0.25, 0.375, 0.5, 0.6125$) and $\text{Ni}_{0.2}\text{Pr}_{0.15}$ and $\text{Mo}_{0.2}\text{Pr}_{0.15}$ catalyst samples. (b) XRD patterns of $\text{Ni}_4\text{Mo}@(\text{Cu}_2\text{O})_y$ ($y = 0, 1, 1.5, 2, 2.5$) catalyst samples.

The TEM images of NiMo , $\text{Ni}_9\text{Mo}_1(\text{Pr}_2\text{O}_3)_{0.375}$, and $\text{Ni}_4\text{Mo}@(\text{Cu}_2\text{O})_y$, together with the corresponding particle size distributions, are presented in Figure 2. It can be seen from Figure 2a,g that the NiMo catalyst is irregularly dispersed, with a particle size range between 6.5 and 6.9 nm, which is significantly higher than those of the $\text{Ni}_9\text{Mo}_1(\text{Pr}_2\text{O}_3)_{0.375}$ and $\text{Ni}_4\text{Mo}@(\text{Cu}_2\text{O})_y$ catalysts (5.5–5.9 nm and 6.0–6.3 nm, respectively). The regions with lattice distribution and amorphous states can be clearly seen in high-resolution TEM (HRTEM) images (Figure 2b). According to fast Fourier-transform (FFT) analysis, the lattice spacing of 0.203 nm is consistent with that of the Ni(111) crystal surface, indicating that the crystalline domain is Ni and the amorphous part is formed through NiMo codoping. The Pr_2O_3 -doped catalyst still has an irregular granular structure after doping, as shown in Figure 2c. According to HRTEM (Figure 2d) observations and FFT analysis, the $\text{Ni}_9\text{Mo}_1(\text{Pr}_2\text{O}_3)_{0.375}$ nanocatalyst has a crystalline structure with a lattice fringe distance of 0.208 nm, which is slightly larger than that of the (111) plane of FCC Ni (0.203 nm), indicating that the presence of the atom of Pr in the crystal lattice of Ni increases the lattice spacing. This is consistent with XRD analysis showing the weakening of the diffraction peak after the addition of Pr. At the same time, the Ni lattice expands and distorts, creating more oxygen defects that trap more electrons at the bottom of the conduction band. It can be seen from the Figure 2e that the Cu-modified NiMo catalyst has a transparent coating at the edge and an amorphous structure inside. The corresponding HRTEM image (Figure 2f), suggests that the lattice spacing of the surrounding transparent particles is 0.19 nm, consistent with that of the crystal surface of Cu_2O (111), which indicates that the shell formed in the catalyst is comprised of Cu_2O . No lattice fringes were observed at the core, indicating that the core is amorphous, which is consistent with the XRD data showing only the diffraction peak of Cu_2O . This implies that a core–shell structure is formed, with NiMo as the nucleus and Cu_2O as the shell. Based on the above analyses, the various modified NiMo nanocatalysts form different structures, which is due to the different configurations of extranuclear electrons in the Pr and

Cu elements. The 5d empty orbit of Pr is a candidate for electron transfer in the synthesized catalyst, which disturbs the Ni electron configuration and causes the crystal shape to change [20,21]. While Ni, Cu, and Mo are transition metals, their different oxidation abilities play an important role in the formation of the structure [25].

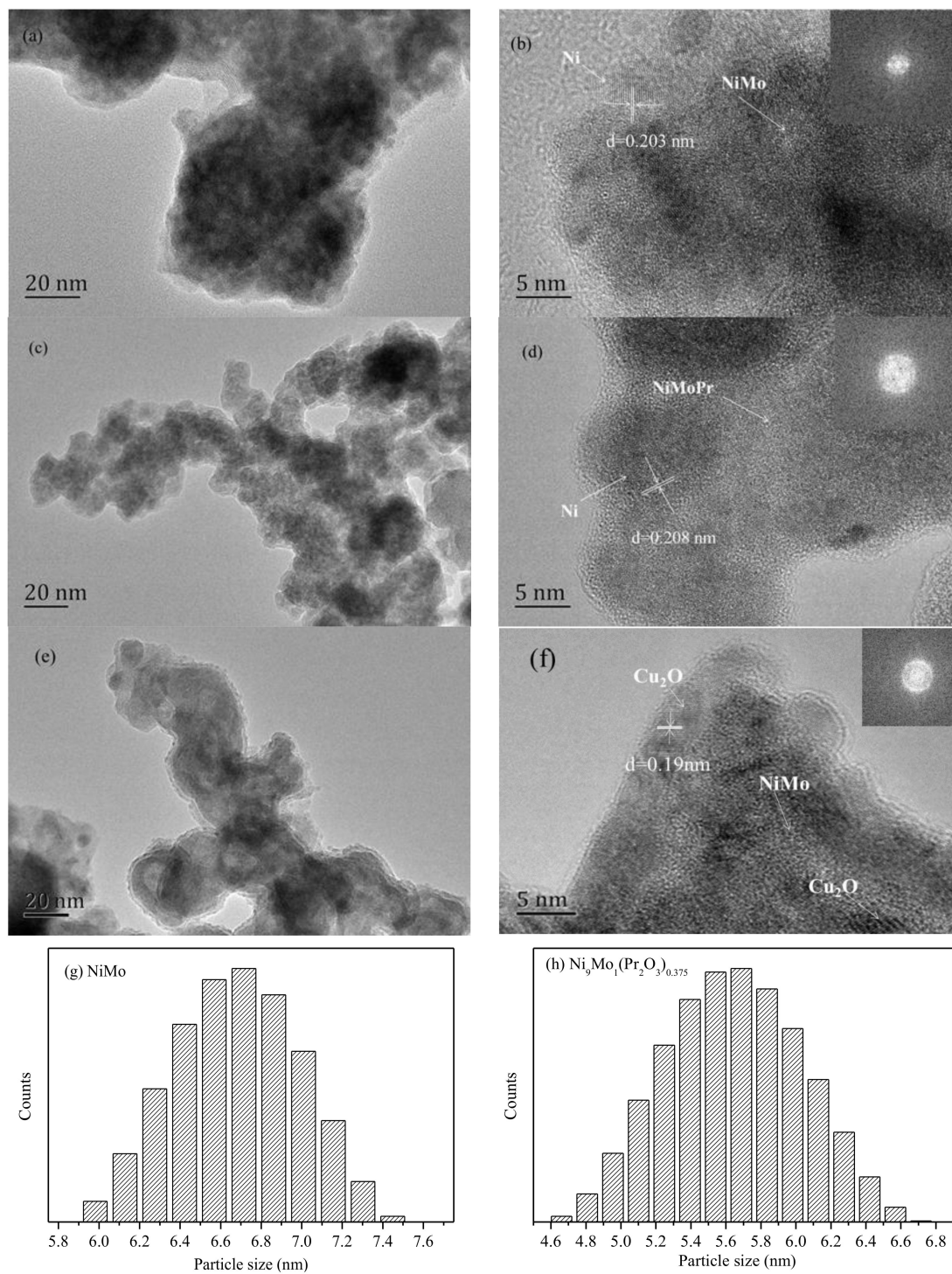


Figure 2. Cont.

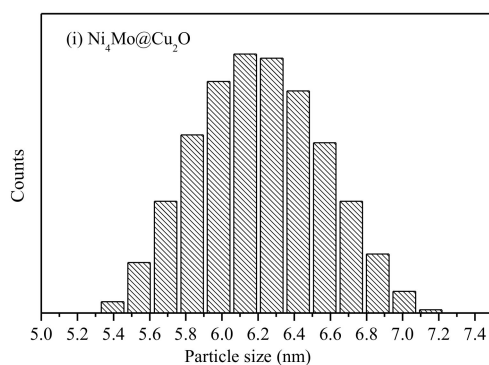


Figure 2. (a) TEM images of Ni_9Mo_1 catalyst, (b) a HRTEM image of Ni_9Mo_1 catalyst, (c) TEM images of $\text{Ni}_9\text{Mo}_1(\text{Pr}_2\text{O}_3)_{0.375}$ catalyst, (d) a HRTEM image of $\text{Ni}_9\text{Mo}_1(\text{Pr}_2\text{O}_3)_{0.375}$ catalyst, (e) TEM images of $\text{Ni}_4\text{Mo}@ \text{Cu}_2\text{O}$ catalyst, (f) a HRTEM image of $\text{Ni}_4\text{Mo}@ \text{Cu}_2\text{O}$ catalyst, (g) metal particles size distribution of Ni_9Mo_1 , (h) metal particles size distribution of $\text{Ni}_9\text{Mo}_1(\text{Pr}_2\text{O}_3)_{0.375}$, and (i) metal particles size distribution of $\text{Ni}_4\text{Mo}@ \text{Cu}_2\text{O}$.

Employing a coreduction strategy to form $\text{Ni}_9\text{Mo}_1(\text{Pr}_2\text{O}_3)_{0.375}$ and $\text{Ni}_4\text{Mo}@ \text{Cu}_2\text{O}$ catalysts yields high-performance structures, which exhibited superior and stable catalytic activity in terms of $\text{N}_2\text{H}_4 \cdot \text{H}_2\text{O}$ selective decomposition to generate H_2 under ambient conditions. However, the mechanistic reason for the catalytic performance enhancement that arises as a result of adding Pr and Cu remains unclear. To gain insight into this mechanism, we conducted X-ray photoelectron spectroscopy (XPS) analysis of the NiMo, $\text{Ni}_9\text{Mo}_1(\text{Pr}_2\text{O}_3)_{0.375}$, and $\text{Ni}_4\text{Mo}@ \text{Cu}_2\text{O}$ catalysts. The XPS spectra of NiMo, $\text{Ni}_9\text{Mo}_1(\text{Pr}_2\text{O}_3)_{0.375}$, and $\text{Ni}_4\text{Mo}@ \text{Cu}_2\text{O}$ in the Ni 2p, Mo 3d, Pr 3d, and Cu 2p regions, respectively, are shown in Figure 3. From the XPS spectra, it is apparent that Ni (Figure 3a) is present in the metallic and oxidation state as NiO and $\text{Ni}(\text{OH})_2$ [20,26]. The main Ni peaks for $\text{Ni}_9\text{Mo}_1(\text{Pr}_2\text{O}_3)_{0.375}$ and $\text{Ni}_4\text{Mo}@ \text{Cu}_2\text{O}$ are positively shifted to higher values, compared to that of undoped NiMo. This suggests that Ni plays an important role in the electron transfer process. Doping with Cu leads to a positive shift in the binding energies of the metallic Ni (Ni 2p_{3/2} 852.6 eV), which may be due to a decrease in the electron density and an increase in metal center d-band vacancies [27,28]. However, after Pr doping, the binding energy of Ni 2p_{3/2} was slightly shifted from 855.3 to 855.8 eV, which indicates that Pr doping of the NiMo catalyst has a less significant effect on Ni binding energy than in the case of $\text{Ni}_4\text{Mo}@ \text{Cu}_2\text{O}$. The Mo species in NiMo (Figure 3b), $\text{Ni}_9\text{Mo}_1(\text{Pr}_2\text{O}_3)_{0.375}$ (Figure 3c), and $\text{Ni}_4\text{Mo}@ \text{Cu}_2\text{O}$ (Figure 3d) are found to exist primarily in the form of oxidation states. Compared with the 3d_{5/2} and 3d_{3/2} peaks that appear at 232.1 and 235.15 eV in NiMo, which are attributed to Mo (VI) species such as MoO_3 and MoO_x , the corresponding peaks for $\text{Ni}_9\text{Mo}_1(\text{Pr}_2\text{O}_3)_{0.375}$ and $\text{Ni}_4\text{Mo}@ \text{Cu}_2\text{O}$ are shifted to higher binding energies, indicating that Mo can act as an electron donor for atoms of Ni and Cu. From Figure 3e, the prominent peak at 932.9 eV is assigned to Pr (III) 3d_{5/2}, indicating that NaBH_4 did not reduce Pr^{3+} to Pr in $\text{Ni}_9\text{Mo}_1(\text{Pr}_2\text{O}_3)_{0.375}$ during catalyst preparation, and the three elements and their oxides are doped with each other to form irregular particles [29,30]. According to the electrode potential, Ni^{2+} can be readily reduced to Ni by NaBH_4 , but it is relatively difficult to reduce Mo^{6+} to Mo, due to the lower reduction potentials of Mo^{6+}/Mo . After the addition of Ni^{2+} and Mo^{6+} , Ni^{2+} is first reduced by NaBH_4 due to its higher potential. However, the oxidizing ability of Cu^{2+} is stronger than that of Ni^{2+} , and Cu^{2+} was reduced first during the reduction, shown in the XPS results in Figure 3f as Cu_2O (Cu 2p 3/2 932.9 eV, Cu 2p 1/2 953.2 eV) and CuO (Cu 2p 3/2 935.4 eV), together with the satellite peaks, while Ni 2p is only shown as Ni (II) [31].

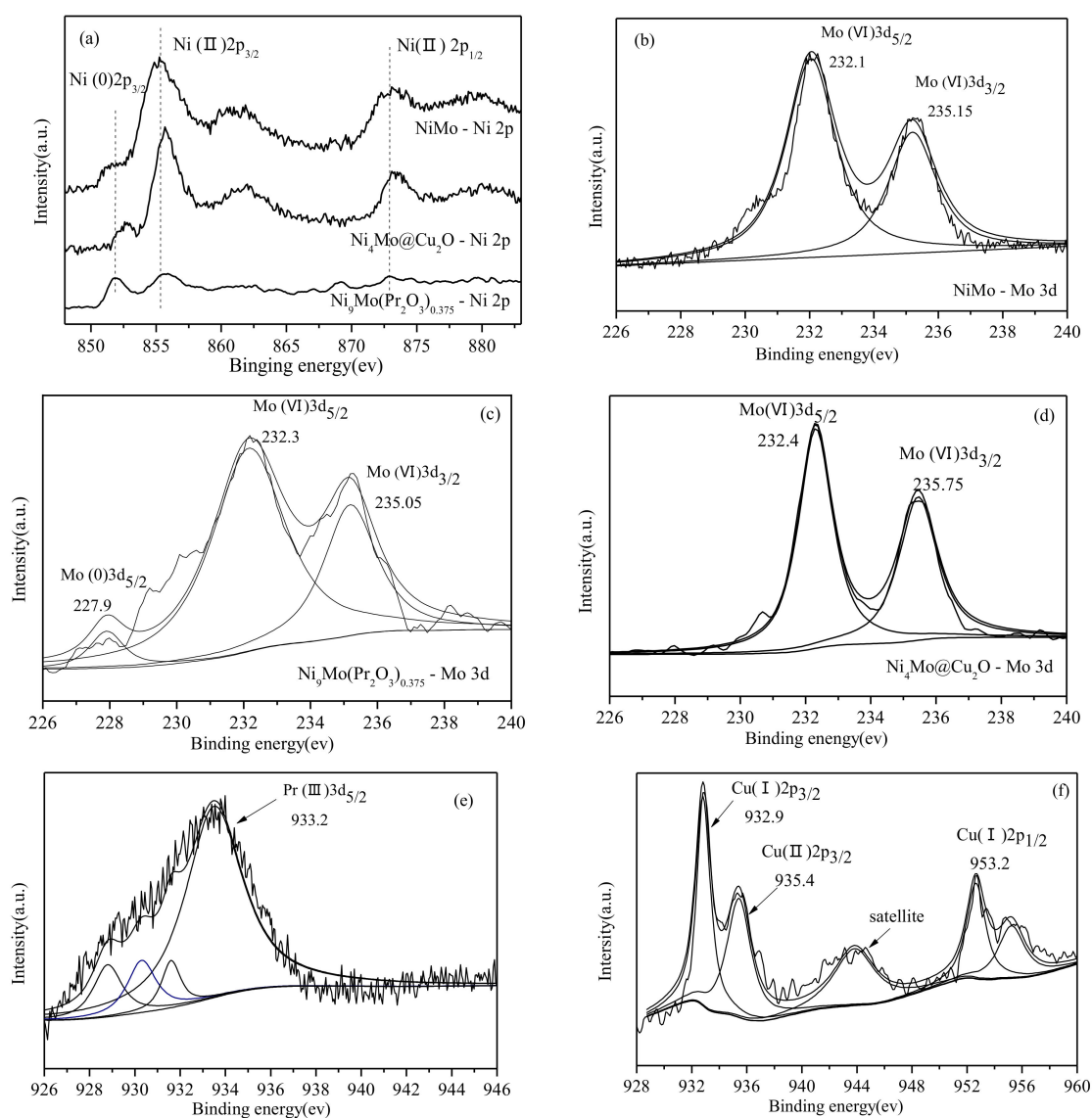


Figure 3. X-ray photoelectron spectra of the as-synthesized Ni_9Mo_1 , $\text{Ni}_9\text{Mo}_1(\text{Pr}_2\text{O}_3)_{0.375}$, and $\text{Ni}_4\text{Mo}@Cu_2O$: (a) Ni 2p, (b), (c), (d) Mo 3d, (e) Pr 3d, and (f) Cu 2p.

2.2. Catalytic Activities of $\text{Ni}_{1-x}\text{Mo}_x(\text{Pr}_2\text{O}_3)_y$ and $\text{Ni}_{1-x}\text{Mo}_x@(\text{Cu}_2\text{O})_y$ Nanocatalysts

The catalytic performances of the as-synthesized nanocatalysts, in terms of hydrogen generation from $\text{N}_2\text{H}_4 \cdot \text{H}_2\text{O}$, are shown in Figure 4. Reactions were initiated by introducing $\text{N}_2\text{H}_4 \cdot \text{H}_2\text{O}$ into the reaction flask with vigorous shaking, at a specified temperature. The catalytic performances of the catalysts were evaluated in a typical water-filled gas burette system. As shown in Figure 4a, elemental nickel and elemental molybdenum have no catalytic activity, and with the increase of NiMo ratio, the catalytic activity appears to initially increase, and then decrease. A NiMo ratio of 9:1 produces the best catalytic effect, with $n(\text{N}_2 + \text{H}_2)/n(\text{N}_2\text{H}_4)$ at 1.9, but the requirement for the highly efficient catalytic hydrogen production of hydrazine hydrate is not achieved. It can be seen from Figure 4b,c that even adding a small amount of Pr or Cu significantly improved the performances of catalysts. When the molar ratios of Ni:Mo:Pr and Ni:Mo:Cu were 9:1:0.75 and 8:2:2, respectively (the total amounts of Ni and Mo were 2 mL, 0.1 mol L^{-1} , respectively), the synthesis of $\text{Ni}_9\text{Mo}_1(\text{Pr}_2\text{O}_3)$ and $\text{Ni}_4\text{Mo}@Cu_2O$ resulted in high hydrogen production efficiency. As shown in Figure 4b, the value of a stoichiometric amount of H_2 and N_2 was 2.8, and the TOF was 62 h^{-1} , for the decomposition of $\text{N}_2\text{H}_4 \cdot \text{H}_2\text{O}$ by $\text{Ni}_9\text{Mo}_1(\text{Pr}_2\text{O}_3)_{0.375}$. Meanwhile, the $\text{Ni}_4\text{Mo}@Cu_2O$ with a core-shell structure produced

a stoichiometric amount of H_2 equal to 2.91 under the same conditions, with a TOF of $71.4 h^{-1}$, which is higher than the majority of reported values shown in Table 1. The excellent catalytic performance of NiMo catalysts doped with Pr_2O_3 or Cu_2O should be primarily attributed to a modification of the electronic structure in the as-synthesized catalysts through interactions between the NiMo and M ($M = Pr_2O_3, Cu_2O$) species, in relation to ligand and strain effects. However, the difference in chemical properties and electronic orbitals between Pr and Cu caused the differences in the catalytic effects of $Ni_9Mo_1(Pr_2O_3)_{0.375}$ and $Ni_4Mo@Cu_2O$. In order to address this issue, further theoretical and experimental research is required to obtain an atomic and molecular-level understanding of the physical and chemical processes involved in the catalytic decomposition of $N_2H_4 \cdot H_2O$ [32].

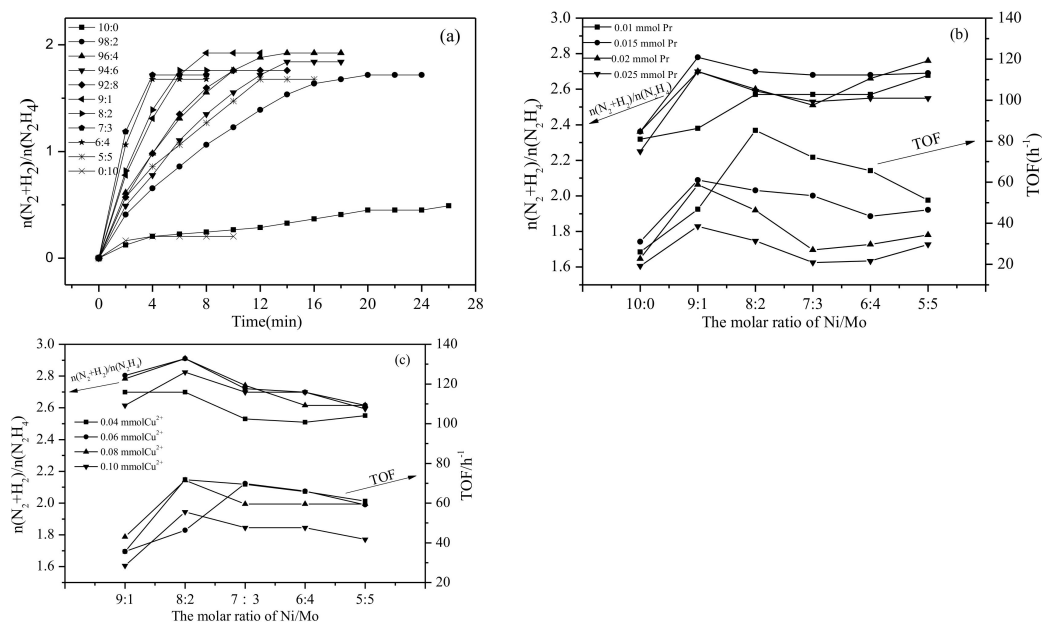


Figure 4. (a) Time-course profiles for the $N_2H_4 \cdot H_2O$ decomposition over the $Ni_{1-x}Mo_x$ catalysts; (b) catalytic performance tests of $NiMo(Pr_2O_3)$ with different molar ratios of NiMo and Pr; and (c) catalytic performance tests of $NiMo@Cu_2O$ with different molar ratios of NiMo and Cu. All the experiments above were done in the presence of 0.2 mL of 10 M $N_2H_4 \cdot H_2O$ and 6 mM NaOH at 343 K.

Table 1. Catalytic activity of different catalysts in hydrazine dehydrogenation.

Catalyst	Temperature(K)	TOF(h^{-1})	E_a ($kJ mol^{-1}$)	Ref.
$Rh_{4.4}Ni/graphene$	298	28	-	[12]
$Ni_{0.9}Pt_{0.1}/Ce_2O_3$	298	28.1	42.3	[33]
$Ni_{1.5}Fe_{1.0}/(MgO)_{3.5}$	299	11	-	[34]
$NiIr_{0.059}/Al_2O_3-HT$	303	12.4	49.3	[17]
$NiPt_{0.057}/Al_2O_3-HT$	303	16.5	34	[16]
$Ni_{0.6}Fe_{0.4}Mo$	323	28.8	50.7	[20]
$Cu@Fe_5Ni_5$	343	11.9	-	[27]
$NiFe/Cu$	343	17.6	45.95	[28]
$Ni_9Mo_1(Pr_2O_3)_{0.375}$	343	62	43.24	This work
$Ni_4Mo@Cu_2O$	343	71.4	46.47	This work

Alkali concentration plays a critical role in promoting the selective decomposition of $N_2H_4 \cdot H_2O$ to generate H_2 . For $N_2H_4 \cdot H_2O$ -based hydrogen generation using $Ni_9Mo_1(Pr_2O_3)_{0.375}$ or $Ni_4Mo@Cu_2O$ catalysts, the optimal alkali concentration was determined to be 6 mM. As shown in Figure 5a, when the concentration of NaOH in the system was 6 mM, the TOF achieved over the $Ni_9Mo_1(Pr_2O_3)_{0.375}$ catalyst was almost ten-fold higher than that obtained in the absence of NaOH, whereas an increase of H_2 selectivity from 25% to 92% was also observed. H_2 selectivity from 25% to 92%, compared with

catalytic system with no added NaOH. Similarly, it can be seen from Figure 5b that the Ni₄Mo@Cu₂O catalyst also showed better performance when 6 mM NaOH was added, where the H₂ selectivity increased to 97% and the TOF increased from 4 h⁻¹ to 71.4 h⁻¹. The hydrogen production rate and H₂ selectivity show no further change with further increases in the Na OH concentration. We surmise that the promoting effects of alkali on both catalytic activity and selectivity might be associated with the enhancement of the reducibility of N₂H₄. As seen in Equations (1) and (2), increasing OH⁻ concentration not only enhances conversion from N₂H₅⁺ to N₂H₄, but is also responsible for decreasing the basic byproduct NH₃, enhancing the selectivity of H₂ [22,32,35]. Furthermore, high concentration of OH⁻ enhanced the hydrolysis of N₂H₄·H₂O, while the decomposition rate of catalytic substrate is improved.

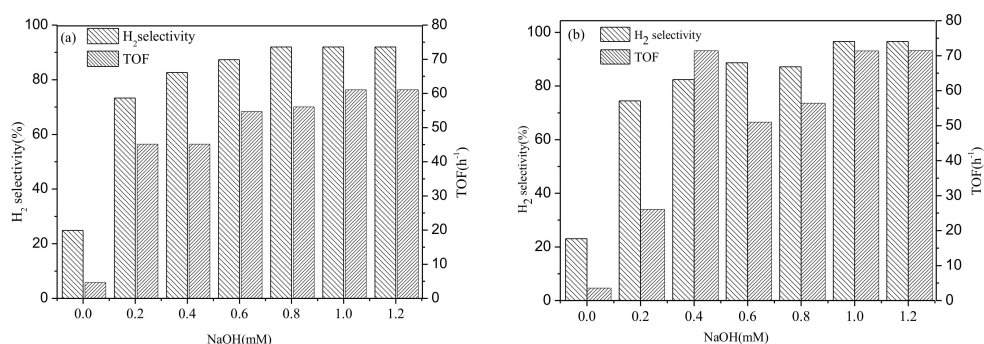
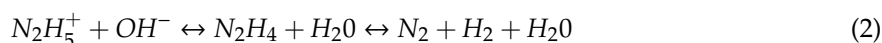


Figure 5. Influence of NaOH concentration on H₂ selectivity and reaction rate of the catalysts (a) Ni₉Mo₁(Pr₂O₃)_{0.375} and (b) Ni₄Mo@Cu₂O.

The N₂H₄·H₂O gas production curve and the Arrhenius diagram of ln(TOF) and 1/T from 298 to 343 K are shown in Figure 6. It can be seen from Figure 6a,c that the catalysts show poor catalytic activity at room temperature, and the gas production rate and hydrogen production of N₂H₄·H₂O increase gradually with increasing reaction temperature. When the reaction temperature is 80 °C, the reaction rate and gas production are not changed, and so a reaction temperature of 70 °C is used in the experiments described in this paper. The Arrhenius plot of ln(TOF) vs. 1/T for our catalysts are plotted in Figure 6b,d, from which the calculated activation energy (E_a) values were 43.24 kJ mol⁻¹ and 46.47 kJ mol⁻¹, for Ni₉Mo₁(Pr₂O₃)_{0.375} and Ni₄Mo@Cu₂O, respectively. This value compares favorably with the literature results for Ni_{0.99}Pt_{0.01} (49.95 kJ mol⁻¹) [14], Ni-Al₂O₃-HT (49.3 kJ mol⁻¹) [36], Ni₈₈Pt₁₂/MIL-101(55.5 kJ mol⁻¹) [10], and the Ni_{0.9}Cr_{0.1} (63.5 kJ mol⁻¹) and Ni_{0.8}W_{0.2} (47.3 kJ mol⁻¹) catalysts [19], indicating that the Ni₉Mo₁(Pr₂O₃)_{0.375} and Ni₄Mo@Cu₂O catalysts have a superior catalytic performance in terms of degrading N₂H₄·H₂O.

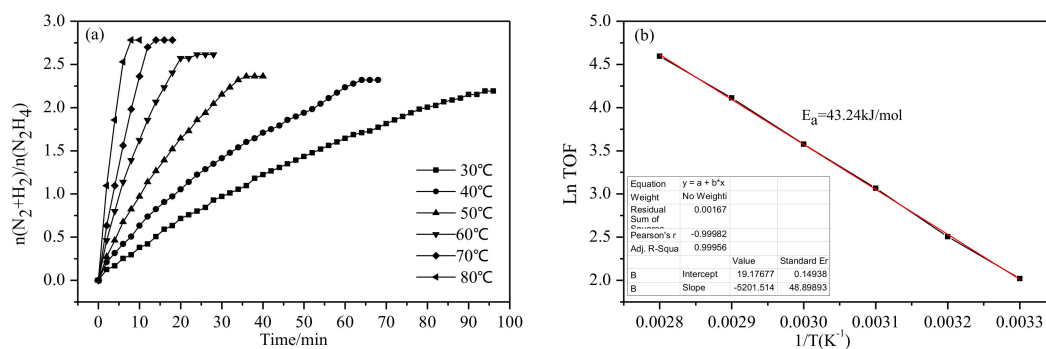


Figure 6. Cont.

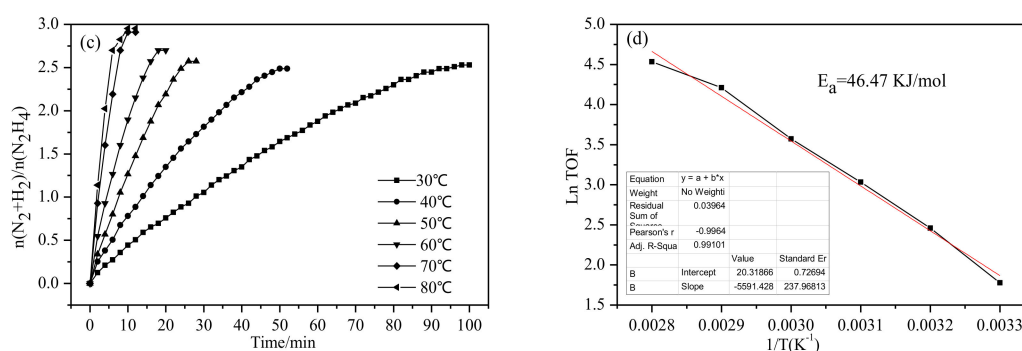


Figure 6. Influence of reaction temperature on the $\text{N}_2\text{H}_4 \cdot \text{H}_2\text{O}$ decomposition at the examined temperature range from 30 °C to 80 °C and Arrhenius treatment of the temperature-dependent rate data for determination of activation energy of the catalysts (a,b) $\text{Ni}_9\text{Mo}_1(\text{Pr}_2\text{O}_3)_{0.375}$ and (c,d) $\text{Ni}_4\text{Mo@Cu}_2\text{O}$.

High durability and stability are crucial to the practical application of a catalyst. Therefore, in the present study, durability tests were performed on $\text{Ni}_9\text{Mo}_1(\text{Pr}_2\text{O}_3)_{0.375}$ and $\text{Ni}_4\text{Mo@Cu}_2\text{O}$ for the same decomposition reaction at 343 K, by adding aqueous hydrous hydrazine (2 mM) to the catalyst after the last reaction round is completed. Time-course plots for the decomposition of $\text{N}_2\text{H}_4 \cdot \text{H}_2\text{O}$ that was catalyzed by $\text{Ni}_9\text{Mo}_1(\text{Pr}_2\text{O}_3)_{0.375}$ are shown in Figure 7a, while Figure 7b shows the corresponding plots for $\text{Ni}_4\text{Mo@Cu}_2\text{O}$. As shown in Figure 7, the catalytic activity of the $\text{Ni}_9\text{Mo}_1(\text{Pr}_2\text{O}_3)_{0.375}$ catalyst exhibits no significant decline even after four rounds of decomposition reactions, indicating that the catalyst is highly stable. However, the $\text{Ni}_4\text{Mo@Cu}_2\text{O}$ catalyst exhibits obvious activity attenuation throughout cyclic usage. We may speculate that this observed activity decay could be attributed to the following possible mechanisms. First, the structure and morphology of the catalysts may have changed because as the number of cycles increases, both the partial agglomeration of metal nanoparticles and amount of exposed active sites decrease. Second, the decay could be caused by the surface oxidation of the catalysts, although as the catalyst is not cleaned by centrifugal separation during the catalytic process, which reduces the area and time of contact of the catalyst with air, this is less likely than the first potential mechanism [37,38].

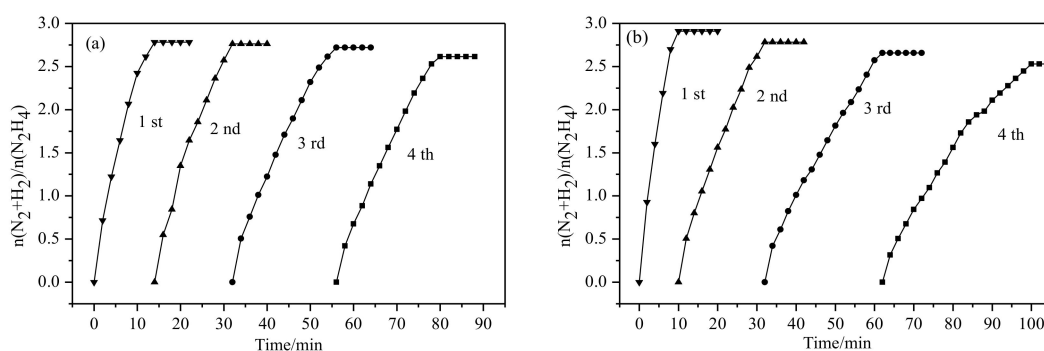


Figure 7. (a) Durability tests of $\text{Ni}_9\text{Mo}_1(\text{Pr}_2\text{O}_3)_{0.375}$ on decomposition of hydrazine at 343 K and (b) durability tests of $\text{Ni}_4\text{Mo@Cu}_2\text{O}$ on decomposition of hydrazine at 343 K.

3. Materials and Methods

3.1. Reagents and Materials

All chemicals were obtained from commercial sources and used without further purification. Nickel (II) chloride hexahydrate ($\text{NiCl}_2 \cdot 6\text{H}_2\text{O}$, Aladdin reagent Co., Ltd., Shanghai, China, >98%), sodium molybdate dehydrate ($\text{Na}_2\text{MoO}_4 \cdot 2\text{H}_2\text{O}$, Tianjin Kemiou Chemical Reagent Co., Ltd., Tianjin, China, 99.5%), praseodymium (III) nitrate hexahydrate ($\text{PrN}_3\text{O}_9 \cdot 6\text{H}_2\text{O}$, Aladdin reagent Co., Ltd., 99%),

copper sulfate pentahydrate ($\text{CuSO}_4 \cdot 5\text{H}_2\text{O}$, Tianjin Kemiou Chemical Reagent Co., Ltd., Tianjin, China, 99%), hydrous hydrazine ($\text{N}_2\text{H}_4 \cdot \text{H}_2\text{O}$, Aladdin reagent Co., Ltd., Shanghai, China, 50%), sodium borohydride (NaBH_4 , Tianjin Fengchuan Chemical Reagent Co., Ltd., Tianjin, China, 99%), and sodium hydroxide (NaOH , Tianjin Kemiou Chemical Reagent Co., Ltd., Tianjin, China, 99%). Ultrapure water was obtained by reversed osmosis followed by ion exchange and filtration.

3.2. Characterization

Powder XRD data were obtained using an X-ray diffractometer with $\text{Cu } k\alpha$ radiation, at an operational voltage and current maintained at 40 kV and 40 mA, respectively. The scanning range for the spectra was $2\theta = 10\text{--}90^\circ$, at a scanning rate of $8^\circ/\text{min}$. The sample morphologies and sizes were analyzed using a JEM-2001F field emission transmission electron microscope, manufactured by JEOL Ltd., Tokyo, Japan. XPS measurements were conducted on an ESCALABMKLL 250Xi spectrometer using an aluminum $k\alpha$ source. The energy of the radiation was $h\nu = 1486.6 \text{ eV}$, while the spectrometer was operated at 12.5 kV and 16 mA. The Ar sputtering experiments were performed under a background vacuum of $8 \times 10^{-10} \text{ Pa}$. The binding energies were calibrated using the C 1 s peak (284.6 eV) of adventitious carbon, and curve fitting was performed using the XPS PEAK 4.1 software. Particle size distribution was measured using a dynamic light scattering nanometer laser particle size analyzer (GS90). The catalyst powder was evenly dispersed in the ultra-pure water by ultrasonic waves before the particle size distribution of the solution was analyzed.

3.3. Synthesis of Ni-Based Catalysts: $\text{Ni}_{1-x}\text{Mo}_x(\text{Pr}_2\text{O}_3)_y$ and $\text{Ni}_{1-x}\text{Mo}_x@(\text{Cu}_2\text{O})_y$

Ni-based nanocatalysts ($\text{Ni}_{1-x}\text{Mo}_x(\text{Pr}_2\text{O}_3)_y$ and $\text{Ni}_{1-x}\text{Mo}_x@(\text{Cu}_2\text{O})_y$) were prepared by a coreduction method. The typical synthesis procedures for $\text{Ni}_9\text{Mo}_1(\text{Pr}_2\text{O}_3)_{0.375}$ and $\text{Ni}_4\text{Mo}@(\text{Cu}_2\text{O})_1$ are described here; 1.8 mL of $\text{NiCl}_2 \cdot 6\text{H}_2\text{O}$ (0.1 mol L^{-1}) and 0.2 mL of $\text{Na}_2\text{MoO}_4 \cdot 2\text{H}_2\text{O}$ (0.1 mol L^{-1}) were added to a round-bottomed flask mixing uniformly, and 0.15 mL of $\text{PrN}_3\text{O}_9 \cdot 6\text{H}_2\text{O}$ (0.1 mol L^{-1}) was then added to the above mixture solution. 1.5 mL of NaBH_4 (0.03 g mL^{-1}) was then quickly added to the above mixture solution for reduction. The reaction solution was vigorously stirred until bubble generation ceased, resulting in the generation of a black suspension of the $\text{Ni}_9\text{Mo}_1(\text{Pr}_2\text{O}_3)_{0.375}$ catalyst, which was directly used in catalytic reactions. For the $\text{Ni}_4\text{Mo}@(\text{Cu}_2\text{O})_1$ catalyst, the same preparation procedure as for $\text{Ni}_9\text{Mo}_1(\text{Pr}_2\text{O}_3)_{0.375}$ was adopted, where 0.8 mL (0.1 mol L^{-1}) of $\text{CuSO}_4 \cdot 5\text{H}_2\text{O}$ was used instead of the $\text{PrN}_3\text{O}_9 \cdot 6\text{H}_2\text{O}$. It is of note that Cu must be added before the $\text{Na}_2\text{MoO}_4 \cdot 2\text{H}_2\text{O}$, where the $\text{Na}_2\text{MoO}_4 \cdot 2\text{H}_2\text{O}$ was alkaline, Cu^{2+} was easily precipitated when it encountered an alkaline solution, and so after adding the $\text{Na}_2\text{MoO}_4 \cdot 2\text{H}_2\text{O}$, NaBH_4 was quickly added to avoid precipitation. $\text{Ni}_{1-x}\text{Mo}_x(\text{Pr}_2\text{O}_3)_y$ and $\text{Ni}_{1-x}\text{Mo}_x@(\text{Cu}_2\text{O})_y$ catalysts with other molar ratios were prepared using the same procedure by adjusting the relative amounts of precursors, and these catalysts were used for characterization tests after vacuum drying.

3.4. Catalysis of Hydrazine Hydrate to Produce Hydrogen

The catalytic reaction of hydrous hydrazine to produce hydrogen by $\text{Ni}_{1-x}\text{Mo}_x(\text{Pr}_2\text{O}_3)_y$ and $\text{Ni}_{1-x}\text{Mo}_x@(\text{Cu}_2\text{O})_y$ were tested at 343 K with vigorous stirring. The catalysts were kept in a 50-mL two-neck round-bottomed flask, one neck was connected to a gas burette to monitor the volume of H_2 released from hydrous hydrazine hydrolysis, while the other neck was used for the introduction of hydrous hydrazine (0.2 mL, 10 mol L^{-1}). In order to maintain the reaction temperature, the flask was placed in a thermostat equipped with a water circulating system, and the reaction was determined to be complete when there was no further gas generation. The molar ratios of $n(\text{metal})/n(\text{N}_2\text{H}_4)$ were theoretically set to 0.11 and 0.14 for the catalytic reactions of $\text{Ni}_9\text{Mo}_1(\text{Pr}_2\text{O}_3)_{0.375}$ and $\text{Ni}_4\text{Mo}@(\text{Cu}_2\text{O})_1$,

respectively. The selectivity towards H₂ generation (X) can be calculated using Equation (3), while the TOF was calculated using Equation (4).

$$X = \frac{3\lambda - 1}{8} \left[\lambda = \frac{n[H_2 + N_2]}{n[N_2H_4]} \right] \quad (3)$$

$$TOF = \frac{n(N_2H_4)_{50\%}}{n(NPs) \cdot t_{50\%}} \quad (4)$$

where TOF refers to the initial turnover frequency, $n(N_2H_4)_{50\%}$ is the amount of hydrous hydrazine when it is half dissolved, n (nanocatalysts) is the mole amount of the metal, and $t_{50\%}$ is the reaction time when conversion reached 50%.

3.5. Durability Testing for the Catalysts

In order to test the durability of the Ni₉Mo₁(Pr₂O₃)_{0.375} and Ni₄Mo@Cu₂O catalysts, after the hydrogen generation reaction was completed the first time, 0.2 mL of hydrazine monohydrate was subsequently added into the reaction flask. Such cycles for testing the N₂H₄·H₂O decomposition of the catalyst were conducted four times at 343 K.

4. Conclusions

In summary, we demonstrated a facile coreduction approach to preparing Pr₂O₃ and Cu₂O-doped NiMo catalysts, without the need for any surfactant or support material, under ambient conditions. The resulting Ni₉Mo₁(Pr₂O₃)_{0.375} and Ni₄Mo@Cu₂O catalysts exhibit good catalytic performances in terms of N₂H₄·H₂O decomposition, which surpassed that of NiMo catalysts that were produced without Pr₂O₃ or Cu₂O doping. The effects of material ratios, NaOH concentration, and reaction temperature on the catalytic efficiency of the catalysts were studied through characterization and catalytic performance evaluation, and compared with unmodified NiMo catalysts. The results show that in the process of modifying NiMo, the NiMoPr₂O₃ is amorphous in structure, and characterized by low crystallinity and an increased number of oxygen vacancies that are beneficial to active site exposure and particle dispersion. NiMo@Cu₂O exhibited a core-shell structure, in which Cu₂O is the shell and NiMo is the core, and the electrons in the core and shell are coupled to each other, with an electron-transfer efficiency that improves catalytic efficiency. Among all the prepared catalysts, Ni₉Mo₁(Pr₂O₃)_{0.375} and Ni₄Mo@Cu₂O showed the highest H₂ selectivity in the presence of 0.2 mL of 10 M N₂H₄·H₂O and 6 mM NaOH at 343 K, with TOFs of 62 h⁻¹ and 71.4 h⁻¹, respectively. These values are higher than the majority of reported results for similar systems. The diameters of these well-dispersed ultrafine catalysts were approximately 5.5–5.9 nm and 6.0–6.3 nm, respectively, lower than that of NiMo catalyst particles (approximately 6.7 nm), which led to an increase in the contact area between N₂H₄·H₂O and the catalyst, and promoted decomposition. This remarkable improvement in the catalytic performance of precious metal-free nanocatalysts demonstrates a promising strategy for future hydrogen production from hydrous hydrazine.

Author Contributions: Conceptualization, Y.L. and N.S.; Methodology, H.Z.; Validation, C.M.; Formal Analysis, H.Z.; Investigation, H.Z.; Writing—Original Draft Preparation, Y.L. and H.Z.; Writing—Review & Editing, Y.L., C.M., and N.S.; Supervision, Y.L. and C.M.; Project Administration, Y.L. and N.S.; Funding Acquisition, Y.L. and C.M.

Funding: This work was kindly supported by the National Natural Science Foundation of China (51508384 and 51508383), the Natural Science Foundation of Tianjin of China (18JCQNJC09000), the Science and Technology Plans of Tianjin of China (17YFCZZC00360), and the Research Fund of the Tianjin Key Laboratory of Aquatic Science and Technology (No. TJKLAST-ZD-2017-03).

Conflicts of Interest: The authors declare no conflicts of interest.

References

1. Chen, P.; Xiong, Z.; Luo, J.; Lin, J.; Lee Tan, K. Interaction of hydrogen with metal nitrides and imides. *Nature* **2002**, *420*, 302–304. [[CrossRef](#)] [[PubMed](#)]
2. Kumaravel, V.; Imam, M.D.; Badreldin, A.; Chava, R.K.; Do, J.Y.; Kang, M.; Abdel-Wahab, A. Photocatalytic hydrogen production: Role of sacrificial reagents on the activity of oxide, carbon, and sulfide catalysts. *Catalysts* **2019**, *9*, 276. [[CrossRef](#)]
3. Zhang, Y.; Heo, Y.J.; Lee, J.W.; Lee, J.H.; Bajgai, J.; Lee, K.J.; Park, S.J. Photocatalytic hydrogen evolution via water splitting: A short review. *Catalysts* **2018**, *8*, 655. [[CrossRef](#)]
4. Du, X.; Cai, P.; Luo, W.; Cheng, G. Facile synthesis of P-doped Rh nanoparticles with superior catalytic activity toward dehydrogenation of hydrous hydrazine. *Int. J. Hydrog. Energy* **2017**, *42*, 6137–6143. [[CrossRef](#)]
5. Pukazhselvan, D.; Kumar, V.; Singh, S.K. High capacity hydrogen storage: Basic aspects, new developments and milestones. *Nano Energy* **2012**, *1*, 566–589. [[CrossRef](#)]
6. De, S.; Zhang, J.; Luque, R.; Yan, N. Ni-based bimetallic heterogeneous catalysts for energy and environmental applications. *Energy Environ. Sci.* **2016**, *9*, 3314–3347. [[CrossRef](#)]
7. Singh, S.K.; Xu, Q. Complete conversion of hydrous hydrazine to hydrogen at room temperature for chemical hydrogen storage. *J. Am. Chem. Soc.* **2009**, *131*, 18032–18033. [[CrossRef](#)] [[PubMed](#)]
8. Zhong, D.C.; Aranishi, K.; Singh, A.K.; Demirci, U.B.; Xu, Q. The synergistic effect of Rh-Ni catalysts on the highly-efficient dehydrogenation of aqueous hydrazine borane for chemical hydrogen storage. *Chem. Commun.* **2012**, *48*, 11945–11947. [[CrossRef](#)] [[PubMed](#)]
9. Zhong, D.C.; Mao, Y.L.; Tan, X.; Zhong, P.; Liu, L.X. RhNi nanocatalyst: Spontaneous alloying and high activity for hydrogen generation from hydrous hydrazine. *Int. J. Hydrog. Energy* **2016**, *41*, 6362–6368. [[CrossRef](#)]
10. Cao, N.; Su, J.; Luo, W.; Cheng, G. Ni-Pt nanoparticles supported on MIL-101 as highly efficient catalysts for hydrogen generation from aqueous alkaline solution of hydrazine for chemical hydrogen storage. *Int. J. Hydrog. Energy* **2014**, *39*, 9726–9734. [[CrossRef](#)]
11. He, L.; Huang, Y.; Wang, A.; Liu, Y.; Liu, X.; Chen, X.; Delgado, J.J.; Wang, X.; Zhang, T. Surface modification of Ni/Al₂O₃ with Pt: Highly efficient catalysts for H₂ generation via selective decomposition of hydrous hydrazine. *J. Catal.* **2013**, *298*, 1–9. [[CrossRef](#)]
12. Du, Y.; Su, J.; Luo, W.; Cheng, G. Graphene-supported nickel-platinum nanoparticles as efficient catalyst for hydrogen generation from hydrous hydrazine at room temperature. *ACS Appl. Mater. Interfaces* **2015**, *7*, 1031–1034. [[CrossRef](#)] [[PubMed](#)]
13. Jiang, Y.; Kang, Q.; Zhang, J.; Dai, H.B.; Wang, P. High-performance nickel-platinum nanocatalyst supported on mesoporous alumina for hydrogen generation from hydrous hydrazine. *J. Power Sources* **2015**, *273*, 554–560. [[CrossRef](#)]
14. Singh, S.K.; Lu, Z.H.; Xu, Q. Temperature-induced enhancement of catalytic performance in selective hydrogen generation from hydrous hydrazine with Ni-based nanocatalysts for chemical hydrogen storage. *Eur. J. Inorg. Chem.* **2011**, *2011*, 2232–2237. [[CrossRef](#)]
15. Singh, S.K.; Iizuka, Y.; Xu, Q. Nickel-palladium nanoparticle catalyzed hydrogen generation from hydrous hydrazine for chemical hydrogen storage. *Int. J. Hydrog. Energy* **2011**, *36*, 11794–11801. [[CrossRef](#)]
16. Bhattacharjee, D.; Mandal, K.; Dasgupta, S. High performance nickel-palladium nanocatalyst for hydrogen generation from alkaline hydrous hydrazine at room temperature. *J. Power Sources* **2015**, *287*, 96–99. [[CrossRef](#)]
17. He, L.; Huang, Y.; Liu, X.Y.; Li, L.; Wang, A.; Wang, X.; Mou, C.Y.; Zhang, T. Structural and catalytic properties of supported Ni-Ir alloy catalysts for H₂ generation via hydrous hydrazine decomposition. *Appl. Catal. B Environ.* **2014**, *147*, 779–788. [[CrossRef](#)]
18. Dai, H.; Zhong, Y.; Wang, P. Hydrogen generation from decomposition of hydrous hydrazine over Ni-Ir/CeO₂ catalyst. *Prog. Nat. Sci. Mater. Int.* **2017**, *27*, 121–125. [[CrossRef](#)]
19. He, L.; Liang, B.; Li, L.; Yang, X.; Huang, Y.; Wang, A.; Wang, X.; Zhang, T. Cerium-oxide-modified nickel as a non-noble metal catalyst for selective decomposition of hydrous hydrazine to hydrogen. *ACS Catal.* **2015**, *5*, 1623–1628. [[CrossRef](#)]
20. Men, Y.; Du, X.; Cheng, G.; Luo, W. CeOx-modified NiFe nanodendrites grown on rGO for efficient catalytic hydrogen generation from alkaline solution of hydrazine. *Int. J. Hydrog. Energy* **2017**, *42*, 27165–27173. [[CrossRef](#)]

21. Manukyan, K.V.; Cross, A.; Rouvimov, S.; Miller, J.; Mukasyan, A.S.; Wolf, E.E. Low temperature decomposition of hydrous hydrazine over FeNi/Cu nanoparticles. *Appl. Catal. A Gen.* **2014**, *476*, 47–53. [[CrossRef](#)]
22. Wang, J.; Li, Y.; Zhang, Y. Precious-metal-free nanocatalysts for highly efficient hydrogen production from hydrous hydrazine. *Adv. Funct. Mater.* **2014**, *24*, 7073–7077. [[CrossRef](#)]
23. Yang, K.; Yao, Q.; Huang, W.; Chen, X.; Lu, Z.H. Enhanced catalytic activity of NiM (M = Cr, Mo, W) nanoparticles for hydrogen evolution from ammonia borane and hydrazine borane. *Int. J. Hydrog. Energy* **2017**, *42*, 6840–6850. [[CrossRef](#)]
24. Zhu, L.L.; Lin, X.M.; Qi, L.J. Preparation and properties for solid solution $\text{Ce}_{0.8}\text{Pr}_{0.2-x}\text{Sm}_x\text{O}_{2-\delta}$ ($x=0.02, 0.05, 0.1$). *Appl. Mech. Mater.* **2015**, *723*, 596–600. [[CrossRef](#)]
25. Yao, Q.; Lu, Z.H.; Zhang, R.; Zhang, S.; Chen, X.; Jiang, H.L. A noble-metal-free nanocatalyst for highly efficient and complete hydrogen evolution from $\text{N}_2\text{H}_4\cdot\text{BH}_3$. *J. Mater. Chem. A* **2018**, *6*, 4386–4393. [[CrossRef](#)]
26. Zhong, Y.J.; Dai, H.B.; Zhu, M.; Wang, P. Catalytic decomposition of hydrous hydrazine over Ni-Pt/La₂O₃ catalyst: A high-performance hydrogen storage system. *Int. J. Hydrog. Energy* **2016**, *41*, 11042–11049. [[CrossRef](#)]
27. Liu, P.; Gu, X.; Wu, Y.; Cheng, J.; Su, H. Construction of bimetallic nanoparticles immobilized by porous functionalized metal-organic frameworks toward remarkably enhanced catalytic activity for the room-temperature complete conversion of hydrous hydrazine into hydrogen. *Int. J. Hydrog. Energy* **2017**, *42*, 19096–19105. [[CrossRef](#)]
28. Zhang, L.; Zhou, L.; Yang, K.; Gao, D.; Huang, C.; Chen, Y.; Zhang, F.; Xiong, X.; Li, L.; Xia, Q. Pd-Ni nanoparticles supported on MIL-101 as high-performance catalysts for hydrogen generation from ammonia borane. *J. Alloy. Compd.* **2016**, *677*, 87–95. [[CrossRef](#)]
29. Devaiah, D.; Thrimurthulu, G.; Smirniotis, P.G.; Reddy, B.M. Nanocrystalline alumina-supported ceria-praseodymia solid solutions: Structural characteristics and catalytic CO oxidation. *RSC Adv.* **2016**, *6*, 44826–44837. [[CrossRef](#)]
30. Devaiah, D.; Tsuzuki, T.; Boningari, T.; Smirniotis, P.G.; Reddy, B.M. $\text{Ce}_{0.80}\text{M}_{0.12}\text{Sn}_{0.08}\text{O}_{2-\delta}$ (M = Hf, Zr, Pr, and La) ternary oxide solid solutions with superior properties for CO oxidation. *RSC Adv.* **2015**, *5*, 30275–30285. [[CrossRef](#)]
31. Wang, H.L.; Yan, J.M.; Li, S.J.; Zhang, X.W.; Jiang, Q. Noble-metal-free NiFeMo nanocatalyst for hydrogen generation from the decomposition of hydrous hydrazine. *J. Mater. Chem. A* **2015**, *3*, 121–124. [[CrossRef](#)]
32. Liu, T.; Yu, J.; Bie, H.; Hao, Z. Highly efficient hydrogen generation from hydrous hydrazine using a reduced graphene oxide-supported NiPtP nanoparticle catalyst. *J. Alloy. Compd.* **2017**, *690*, 783–790. [[CrossRef](#)]
33. Wang, H.L.; Yan, J.M.; Wang, Z.L.; O, S.L.; Jiang, Q. Highly efficient hydrogen generation from hydrous hydrazine over amorphous Ni_{0.9}Pt_{0.1}/Ce₂O₃ nanocatalyst at room temperature. *J. Mater. Chem. A* **2013**, *1*, 14957–14962. [[CrossRef](#)]
34. Gao, W.; Li, C.; Chen, H.; Wu, M.; He, S.; Wei, M.; Evans, D.G.; Duan, X. Supported nickel-iron nanocomposites as a bifunctional catalyst towards hydrogen generation from $\text{N}_2\text{H}_4\cdot\text{H}_2\text{O}$. *Green Chem.* **2014**, *16*, 1560–1568. [[CrossRef](#)]
35. He, L.; Huang, Y.; Wang, A.; Wang, X.; Zhang, T. H₂ production by selective decomposition of hydrous hydrazine over Raney Ni catalyst under ambient conditions. *AIChE J.* **2013**, *59*, 4297–4302. [[CrossRef](#)]
36. He, L.; Huang, Y.; Wang, A.; Wang, X.; Chen, X.; Delgado, J.J.; Zhang, T. A noble-metal-free catalyst derived from Ni-Al hydrotalcite for hydrogen generation from $\text{N}_2\text{H}_4\cdot\text{H}_2\text{O}$ decomposition. *Angew. Chem. Int. Ed.* **2012**, *51*, 6191–6194. [[CrossRef](#)] [[PubMed](#)]
37. Dai, H.; Qiu, Y.P.; Dai, H.B.; Wang, P. A study of degradation phenomenon of Ni–Pt/CeO₂ catalyst towards hydrogen generation from hydrous hydrazine. *Int. J. Hydrog. Energy* **2017**, *42*, 16355–16361. [[CrossRef](#)]
38. Dai, H.; Dai, H.B.; Zhong, Y.J.; Kang, Q.; Sun, L.X.; Wang, P. Kinetics of catalytic decomposition of hydrous hydrazine over CeO₂-supported bimetallic Ni–Pt nanocatalysts. *Int. J. Hydrog. Energy* **2017**, *42*, 5684–5693. [[CrossRef](#)]

